Journal of Electronic Materials (2024) 53:3438–3449
https://doi.org/10.1007/s11664-024-11134-5

ORIGINAL RESEARCH ARTICLE

High Thermoelectric Performance of Ge–Sb–Te Nanosheets: A Density Functional Study

Jing Tian[1,2] · Weiliang Ma[1,2,3] · Marie-Christine Record[2] · Pascal Boulet[1]

Received: 8 January 2024 / Accepted: 19 April 2024 / Published online: 17 May 2024

Abstract

This paper reports first-principles calculations on nanosheets of Ge–Sb–Te compounds, namely Sb_2Te_3, $GeSb_2Te_4$ and $Ge_2Sb_2Te_5$ under two crystalline atomic stakings S1 and S2. Sb_2Te_3, $GeSb_2Te_4$ and $Ge_2Sb_2Te_5$-S1 are semiconductors with a narrow band gap ranging between 0.7 and 0.74 eV as evaluated with the HSEsol functional. The transport properties have been investigated by Boltzmann transport theory together with deformation potential theory. The strain effects on their electronic and thermoelectric properties as well as on their dynamical properties have been investigated. A valence band convergence is found in the equilibrium structures, which is an efficient approach to improve the thermoelectric performance of materials. Sb_2Te_3, $GeSb_2Te_4$ and $Ge_2Sb_2Te_5$-S1 possess high TE performance in a wide range of temperature, and the highest values of zT are 2.94, 2.63 and 2.27, respectively.

Keywords Layered chalcogenide · thermoelectricity · Boltzmann transport · density functional theory

Introduction

Thermoelectric (TE) materials that offer direct electrothermal energy conversion have garnered significant research interest in the fields of waste heat recovery,[1-3] power generation[4,5] and on-chip cooling,[6] enabling a new route for the harvesting of green and clean energy to address the global energy crisis. Benefitting from flexible size, light weight, high reliability, fast response, long duration and no pollutants, TE materials have attracted remarkable attention. However, the applications of TE materials have been hindered by the low energy conversion efficiency.[7] The energy conversion efficiency of TE materials is characterized by the figure of merit $zT = S^2\sigma T/\kappa$ where S is the Seebeck coefficient, σ is the electrical conductivity, κ is the thermal conductivity and T is the temperature. The thermal conductivity κ consists of two parts: the electronic part, κ_e, contributed by the electron transport and the lattice part, κ_l, contributed by the lattice vibrations.

Two popular strategies have spurred the enhanced figure of merit (zT): complex structures and low-dimensional structures. It has been proposed that low-dimensional nanostructures can introduce a quantum confinement effect,[8] which effectively increases the Seebeck coefficient and reduces the thermal conductivity, thereby enhancing the efficiency of thermoelectric devices. Nano-2D transition metal dichalcogenides, such as MoS_2,[9,10] WS_2,[11] $MoSe_2$,[12] and WSe_2,[13] are semiconductors with large band gaps (1–2 eV), possessing a promising zT value ranging from 0.8 to 2.1. A nanostructured Bi_2Te_3/Sb_2Te_3 superlattice with alternative layer thickness of 1 nm and 5 nm for Bi_2Te_3 and Sb_2Te_3, respectively, is reported to have impressive zT values at 300 K of 2.4 and

Weiliang Ma, Marie-Christine Record, and Pascal Boulet have contributed equally to this work.

✉ Marie-Christine Record
m-c.record@univ-amu.fr

Jing Tian
jing.tian@etu.univ-amu.fr

Weiliang Ma
weiliang.ma@univ-lorraine.fr

Pascal Boulet
pascal.boulet@univ-amu.fr

1 Department of Chemistry, University of Aix-Marseille, MADIREL, Avenue Normandie-Niemen, Marseille F-13013, France

2 Department of Chemistry, University of Aix-Marseille, IM2NP, Avenue Normandie-Niemen, Marseille F-13013, France

3 Present Address: IJL Institute, University of Lorraine, Campus Artem, 2 allée André Guinier, BP 50840, 54011 Nancy Cedex, France

1.5 for *p*-type and *n*-type,[14] respectively, whereas the pure Sb_2Te_3 film exhibits a zT of 0.26 at 300 K.[15]

Numerous materials belonging to the IV-VI and V_2-VI_3 families exhibit high TE performance. These include lead chalcogenides,[16] Bi_2Te_3-based alloys,[17] and recently discovered compounds such as SnSe[18] and GeTe.[19] Additionally, there exists a series of ternary compounds in the form of $A^{IV}B^{VI}$-$A^{V}_2B^{VI}_3$ systems (where A^{IV} represents Ge, Sn or Pb; A^{V} stands for Bi or Sb; and B^{VI} indicates Te or Se). These ternary compounds can be conceptualized as pseudo-binary alloys. Notably, among these materials, Ge–Sb–Te (GST)-based compounds, which are renowned for their outstanding properties as phase-change materials used in information storage and retrieval applications, have been shown to exhibit excellent TE performance, with zT values ranging from 0.3 to 0.71.[20-23]

Xu et al.[24] conducted a study on a Sb_2Te_3 nanosheet using density functional theory (DFT) and the semiclassical Boltzmann transport theory. They identified optimal zT values at moderate temperatures, reaching approximately 0.782 for a carrier concentration of 2.0×10^{19} cm^{-3} at 800 K. Notably, the zT values calculated for this nanosheet far surpass those of Sb_2Te_3 nanomaterials, bulk Sb_2Te_3 and eutectic PbTe-Sb_2Te_3 composites. In a recent study using DFT, Fang et al.[25] investigated 2D $GeSb_2Te_4$, which possesses a narrow band gap of 0.80 eV. Considering relaxation time, they observed *n*-type power factors as high as 7.4 mW/(K m^2). These findings resulted in elevated zT values, reaching 1.60 at 300 K and further increasing to 3.80 at 700 K. This suggests that low-dimensional structures indeed offer superior thermoelectric performance for this materials family. Most of the theoretical investigations on the Ge–Sb–Te-type nanosheets have been reported separately. Because of the calculation benchmark differences, it is difficult to compare the TE properties. In this paper, we studied the stability, vibrational properties and thermoelectric figure of merit of two-dimensional materials of the Ge–Sb–Te family, namely Sb_2Te_3, $GeSb_2Te_4$ and $Ge_2Sb_2Te_5$ nanosheets. We have also explored the effect of biaxial strains on their properties. We note that, both in the cited literature and in our present work, nanosheets stand for monolayers.

Computational Details

The DFT calculations presented here are based on plane-wave basis sets, using the projector-augmented wave (PAW) method[26] as implemented in the VASP code.[27,28] The revised Perdew–Burke–Ernzerhof functional for solids (PBEsol)[29] within the generalized gradient approximation (GGA) is used in these calculations to describe the exchange and correlation interactions. For all the structures studied in this work, the plane wave cutoff energy is set to 600 eV and the Gaussian smearing is 0.01 eV. The total energy and atomic forces convergence thresholds have been defined as 10^{-8} eV and 10^{-3} eV $Å^{-1}$, respectively. The nanosheets were cleaved from a totally relaxed bulk crystal along the (001) plane. A nanosheet slab expanded to a $4 \times 4 \times 1$ supercell together with a top vacuum layer was used to calculate the interatomic forces, within the density functional perturbation theory (DFPT),[30] that were further processed by the Phonopy[31,32] and Phono3py[31,32] packages to obtain the phonon band structure and lattice thermal conductivity. The Brillouin zone (BZ) has been sampled with the Monkhorst-Pack division scheme. K-point meshes of $15 \times 15 \times 3$, $15 \times 15 \times 3$, $15 \times 15 \times 5$ and $15 \times 15 \times 5$ were applied to the conventional cells for bulk Sb_2Te_3, $GeSb_2Te_4$ and $Ge_2Sb_2Te_5$ with stacking 1 and 2, respectively. K-point meshes of $15 \times 15 \times 1$ and $3 \times 3 \times 1$ were applied to the nanosheets and all supercells, respectively. The lattice thermal conductivity has been calculated by using both a full solution of the linearized phonon Boltzmann equation (LBTE) method as introduced in Ref.[33] and the Boltzmann transport equation within the relaxation time approximation (RTA). The spectral representation of the dynamical thermal conductivity obtained from the LBTE method is $\kappa_1 = \int d\omega' \frac{\rho(\omega')}{\omega' - i\omega'}$, where $\rho(\omega')$ is the spectral density. Furthermore, because the lattice thermal conductivity is an intensive property of bulk materials, that of two-dimensional material should be normalized by multiplying by L_z/d,[34] where L_z is the lattice parameter c and d is the thickness of the nanosheets.

The electron transport properties have been calculated by solving the Boltzmann semi-classical transport equation as implemented in the BoltzTraP2[35] code based on the use of a full band structure in the BZ. The program can read in energy states at each k-point from VASP output and then rebuild the full BZ band structure. The sampling, which is important in transport calculation, has been performed with a very dense k-point mesh of $81 \times 81 \times 1$ for Sb_2Te_3, $GeSb_2Te_4$ and $Ge_2Sb_2Te_5$ with stacking 1 and 2. For the calculation of the electronic part κ_e of the thermal conductivity and the electrical conductivity σ that both depend on τ, the τ value must be evaluated independently. By using the deformation potential (DP) theory[36] with the effective mass approximation, the mobility μ of 2D materials can be defined as:[37]

$$\mu_{2D} = \frac{2e\hbar^3 C_{2D}}{3k_B T|m^*|E_d^2} \tag{1}$$

where e is the electron charge, $\hbar$ is the reduced Planck constant, C_{2D} is the elastic constant, k_B is the Boltzmann constant, T is the temperature, m^* is the effective mass and E_d is the deformation potential expressed as $E_d = \partial E/\partial(\Delta a/a_0)$, where E is the energy of conduction band minimum (CBM) or valence band maximum (VBM), and a_0 is the equilibrium lattice constant. Then, we can evaluate τ from $\tau = (\mu m^*)/e$,

where the effective mass is derived from the second derivative of E: $m^*_{k,l} = \hbar^2/(\partial^2 E/\partial k_k \partial k_l)$.

Biaxial strains, both tensile and compressive, have been applied to the nanosheets. The strains range between -3% (compressive) and +3% (tensile) and are calculated as $(a - a_0)/a_0 \times 100$, where a_0 is the lattice parameter of the unstrained structure.

To gain insight into the bonding features of the structures, several tools have been used, namely the electron localization function,[38] the Bader analysis of the electron density[39] and the crystal orbital Hamiltonian population analysis.[40] The pertaining calculations have been performed with VASP, Critic2[41] and Lobster,[42] respectively. The visualization of the structures has been performed with Vesta.[43]

Results

Structural Information

Layered structures of Sb_2Te_3, $GeSb_2Te_4$ and $Ge_2Sb_2Te_5$ with stacking 1 (S1) and $Ge_2Sb_2Te_5$ with stacking 2 (S2) crystallize in hexagonal cells contributed by three 5-atom-layered slabs, three 7-atom-layered slabs, and one 9-atom-layered slab, respectively (as shown in Fig. S1, see online supplemental material). Two stacking sequences of $Ge_2Sb_2Te_5$ have been considered, where the in-layer germanium and antimony are interchanged. The slabs are held together by van der Waals interactions. With an exfoliation energy of about 25 meV/Å^2, weak-interaction Te-based compounds should be exfoliable materials, which has been observed for the bulk Bi_2Te_3 and Sb_2Te_3.[44]

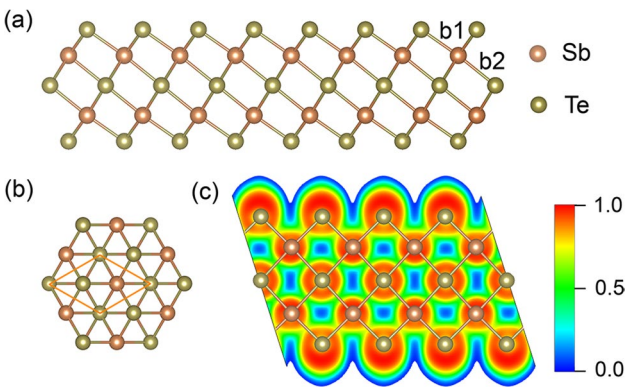

Fig. 1 Structure of Sb_2Te_3 nanosheet (monolayer). (a) Side view, (b) top view, (c) electronic localization function (ELF).

In this study, to benefit from quantum-well effects, four nanosheet structures, depicted in Figs. 1 and S2, have been modeled. These nanosheet structures correspond to one slab of the corresponding bulk compound. To avoid spurious interaction between adjacent layers, Sb_2Te_3, $GeSb_2Te_4$ and $Ge_2Sb_2Te_5$-S1 and -S2 nanosheets have been optimized with an on top vacuum thickness of 20 Å, 20 Å, 22 Å and 22 Å, respectively.

The equilibrium lattice constants of the four nanosheets have been calculated using the PBEsol-GGA functional without spin-orbit coupling (SOC), which shows a minor effect on the geometry.[45] Both the nanosheet lattice constants and the atomic positions therein have been fully relaxed. The lattice constant c of nanosheets comprises the vacuum height and the slab thickness. To model the nanosheets, the bulk structures need to be optimized first and the results are listed in Table I. In this table, for the bulk, the slab thickness corresponds to the distance between the bottom atom and the top one of the constitutive slab of the bulk (see Fig. S3). For the bulk structure of Bi_2Te_3, the optimized lattice constants are $a = 4.27$ Å and $c = 29.98$ Å, which are in good agreement with the reported experimental values ($a = 4.26$ Å,[46] 4.24 Å,[47] and $c = 30.19$ Å[47]). Similarly, the calculated lattice constants of $GeSb_2Te_4$ is close to the experimental value of $a = 4.21$ Å.[46] From 3D to 2D, the lattice constant a of the four nanosheets is slightly contracted, while the thickness is expanded. Because of the absence of bonding

Table I Characteristic lengths (lattice parameters, bond lengths and slab thickness), in angström units, of bulk Sb_2Te_3, $GeSb_2Te_4$, $Ge_2Sb_2Te_5$ -S1 and $Ge_2Sb_2Te_5$-S2 and corresponding nanosheets calculated with the PBEsol functional.

	a	c	Slab thickness	Bond length b1	b2	b3	b4
Bulk							
Sb_2Te_3	4.27	29.98	7.32	3.00	3.15		
$Ge_2Sb_2Te_4$	4.24	40.50	10.73	2.99	3.16	2.96	
$Ge_2Sb_2Te_5$-S1	4.22	16.83	14.11	2.98	3.16	2.94	2.97
$Ge_2Sb_2Te_5$-S2	4.22	16.88	14.28	2.80	3.17	2.99	3.14
Nanosheet							
Sb_2Te_3	4.24	27.40	7.34	2.98	3.14		
$GeSb_2Te_4$	4.23	30.73	10.72	2.97	3.16	2.95	
$Ge_2Sb_2Te_5$-S1	4.21	34.27	14.17	2.96	3.16	2.93	2.98
$Ge_2Sb_2Te_5$-S2	4.18	34.79	14.49	2.79	3.17	2.98	3.15

interaction on the vacuum side, the outermost bond length of the nanosheets decreased.

To give a full picture of bonding trend of both bulk and nanosheets, we calculated the topological properties of bond critical points (BCPs) within the approach of the quantum theory of atoms in molecules (QTAIM).[48] The results are gathered in Table II and the evolution of the bond degree H/ρ with respect to the dimensionless $|V|/G$ ratio is depicted in Fig. S4. The topological properties of the bulk structures at the BCPs are listed in Table II for comparison. The position of the BCPs is shown in Figs. 1, S1 and S2. In Table II, $r1$ and $r2$ are the distances between the BCP and the two corresponding bond ends, the angle is measured between the BCP and the two bond ends, ρ and $\nabla^2\rho$ are the electron charge density and its Laplacian at the BCPs, and G, V and H represent the kinetic, potential and total energy densities at the BCPs. As in the nanosheets there is no Te-Te interlayer interaction, the results obtained for this type of bond for the bulk structures are not presented in this section. Usually, closed shell interactions (ionic, H-bonds and vdW) have a large positive value of $\nabla^2\rho$ over the entire interaction region, $|V|/G < 1$ and a small ρ. Conversely, $\nabla^2\rho < 0$, $|V|/G > 2$ and a large ρ are expected for shared interactions (covalent or polar bonds).[49] In all the nanosheets of interest, the bonds are neither pure ionic bonds nor pure covalent ones. There is no electron accumulation along the bonds as evidenced by the positive Laplacian values at the BCPs (Table II) and the electron localization function (ELF) shown in Figs. 1, and S2. In addition, it can be found that the $|V|/G$ ratio of b1 BCPs in nanosheets is larger than that in bulk, indicating an edge effect with a stronger ionic interaction in low-dimensional structures.

For all the structures except $Ge_2Sb_2Te_5$-S2, b1 bears the highest $|V|/G$ value compared with b2, b3 and b4, which should reflect a lower ionic character of b1. In the case of $Ge_2Sb_2Te_5$-S2, the highest $|V|/G$ value is associated with b3 and is the same as that of b1 in $Ge_2Sb_2Te_5$-S1. We note that both the b1 and b3 BCPs are located at the slab edge. Indeed, in $Ge_2Sb_2Te_5$-S2 the outermost bond ends are Te and Ge whereas those in the other structures are Te and Sb. The lowest $|V|/G$ value is associated with b4 in $Ge_2Sb_2Te_5$-S2 and b2 in $Ge_2Sb_2Te_5$-S1. These bonds are located in the middle of the slab. Both the $|V|/G$ and the electron density $\rho(r)$ at the bond critical points decrease monotonically across the $Ge_2Sb_2Te_5$-S1 and $Ge_2Sb_2Te_5$-S2 slab from the edge to the middle. This is in contrast with the electron density fluctuation observed across the nanosheet of $Pb_2Bi_2Te_5$.[50]

On the other hand, bond strength also plays a pivotal role in determining the lattice thermal conductivity κ_l of materials. Zhang[51] found a strong positive correlation between the anisotropy in lattice thermal conductivity and the anisotropy in electron charge density. We conducted a chemical bond analysis using the crystal orbital Hamilton population (COHP) method to provide insights into the bond strength within the solids. The projected COHP (pCOHP) is shown in Fig. S5. Integrated values IpCOHP (including bonding and antibonding contributions) were employed to evaluate bond strength. As illustrated in Fig. S5 the calculated IpCOHP average value increases from $Ge_2Sb_2Te_5$-S1 to $GeSb_2Te_4$ to Sb_2Te_3. As stronger bonds exhibit greater orbital overlap, the $Ge_2Sb_2Te_5$-S1 nanosheet bears weaker (softer) bonding interactions than the other structures. Hence, in accordance with Slack's theory,[52] the $Ge_2Sb_2Te_5$-S1 nanosheet should bear lower κ_l.

Dynamic Properties

Dynamic properties play an important role in low-dimensional materials for structural stability. Phonon dispersion has been determined to assess the stability of specific materials. Figures 2a and S6 show that all four nanosheets are dynamically stable with no imaginary modes through the

Table II Topological properties at the BCPs of Sb_2Te_3, $GeSb_2Te_4$, $Ge_2Sb_2Te_5$-S1 and $Ge_2Sb_2Te_5$-S2 nanosheets. The position of the BCPs is shown in Figs. 1 and S2. $r1$ and $r2$ in Å; Angle in degrees; ρ and $\nabla^2\rho$ in units of 10^{-2} e/bohr^3 and 10^{-2} e/bohr^5; G, V and H in units of 10^{-2} a.u./bohr^3.

BCP	$r1$	$r2$	Angle	ρ	$\nabla^2\rho$	G	V	H	$\lvert V\rvert/G$	H/ρ
Sb_2Te_3-b1	2.930	2.703	179.26	4.682	1.286	1.960	− 3.599	− 1.639	1.836	− 0.350
Sb_2Te_3-b2	2.871	3.058	179.63	3.507	2.360	1.472	− 2.355	− 0.882	1.599	− 0.252
$GeSb_2Te_4$-b1	2.919	2.691	179.33	4.768	1.237	2.006	− 3.703	− 1.697	1.846	− 0.356
$GeSb_2Te_4$-b2	3.076	2.895	179.83	3.386	2.356	1.410	− 2.231	− 0.821	1.582	− 0.243
$GeSb_2Te_4$-b3	3.009	2.568	179.57	3.867	1.772	1.565	− 2.687	− 1.122	1.717	− 0.290
$Ge_2Sb_2Te_5$-S1 b1	2.686	2.914	179.31	4.797	1.231	2.023	− 3.739	− 1.716	1.848	− 0.358
$Ge_2Sb_2Te_5$-S1 b2	2.902	3.080	179.72	3.354	2.362	1.395	− 2.200	− 0.805	1.577	− 0.240
$Ge_2Sb_2Te_5$-S1 b3	2.548	2.992	179.51	3.988	1.683	1.617	− 2.813	− 1.196	1.740	− 0.300
$Ge_2Sb_2Te_5$-S1 b4	2.596	3.030	179.97	3.704	1.848	1.490	3− 2.518	− 1.028	1.690	− 0.278
$Ge_2Sb_2Te_5$-S2 b1	2.715	2.923	179.53	4.631	1.442	1.955	− 3.550	− 1.595	1.816	− 0.344
$Ge_2Sb_2Te_5$-S2 b2	2.889	3.066	179.87	3.446	2.331	1.436	− 2.290	− 0.853	1.594	− 0.248
$Ge_2Sb_2Te_5$-S2 b3	2.471	2.793	178.83	5.063	1.398	2.222	− 4.095	− 1.873	1.843	− 0.370
$Ge_2Sb_2Te_5$-S2 b4	3.163	2.830	177.29	2.632	2.442	1.076	− 1.541	− 0.465	1.432	− 0.177

whole Brillouin zone. However, DFT calculation with GGA functionals may overestimate the lattice constants, leading to DFPT-calculated small negative modes. To give a precise description of the stability, we calculated the Gibbs free energy with the quasi-harmonic approximation (QHA) approach:

$$G(P,V) = E(V)_{0K} + F_{vib}(T) + F_{el}(T,V) + PV \quad (2)$$

where $E(V)_{0K}$ is the 0K energy, $F_{vib}(T)$ is the vibrational free energy and $F_{el}(T,V)$ is the electronic free energy at volume V and temperature T and P is the pressure. The summations of the first three terms are usually referred to as Helmholtz free energy. The vibrational free energy reads:[53]

$$F_{vib}(T) = \frac{1}{2}\sum_{k,v}\hbar\omega(k,v) + k_b T\sum_{k,v}\ln\left(1-\exp\frac{\hbar\omega(k,v)}{k_b T}\right) \quad (3)$$

where $\omega(k,v)$ is the phonon frequency of the k^{th} vector. The Gibbs energy has been calculated at atmospheric pressure and different temperatures by selecting the minimum value for each volume change (orange lines in Fig. S7). The calculated Gibbs free energy of the four nanosheets are negative, indicating their stability.

Based on Slack's theory,[52] there are four criteria for finding crystals with low thermal conductivity: (1) high atomic mass, (2) weak interatomic bonds, (3) complex crystal structures and (4) high anharmonicity. Compared with Pb-based chalcogenides, we have replaced the toxic heavy element Pb with the environmentally friendly Ge and heavy element Bi with the more sustainable element Sb. The lattice thermal conductivity is evaluated by solving the Boltzmann transport equation (BTE) with the LBTE and relaxation time approximation (RTA) methods. The lattice thermal conductivities of Ge–Sb–Te nanosheets are higher than those of Pb–Bi–Te ones.[45] From the LBTE method, the κ_l in the a direction at room temperature of Sb_2Te_3, $GeSb_2Te_4$, $Ge_2Sb_2Te_5$-S1 and $Ge_2Sb_2Te_5$-S2 are 4.34 W $m^{-1}K^{-1}$, 2.67 W $m^{-1}K^{-1}$, 1.89 W $m^{-1}K^{-1}$, 2.91 W $m^{-1}K^{-1}$, respectively, and at 700 K they amount to 1.85 $Wm^{-1}K^{-1}$, 1.15 W $m^{-1}K^{-1}$, 0.81 W $m^{-1}K^{-1}$, 1.25 W $m^{-1}K^{-1}$, respectively. It is noticeable that for $Ge_2Sb_2Te_5$-S1, the lattice thermal conductivity is larger than that of the bulk.[54] This behavior has already been observed in other similar materials.[55] According to these authors, the increase of the lattice thermal conductivity results from the enhancement of the in-plane phononic transport after the van der Waals interactions disappear between neighboring layers.

From the atom-decomposed phonon DOS (Fig. 2a) and the accumulated lattice thermal conductivity (Fig. S8), we found that the frequencies ranging from 0 to 2 Thz contribute up to 81.2% to the lattice heat transport for Sb_2Te_3. A similar situation has been found in the nanosheets of $Ge_2Sb_2Te_5$-S2, whereas the lattice thermal conductivity of $GeSb_2Te_4$ and $Ge_2Sb_2Te_5$-S1 shows an approximate linear behavior with the frequency. Both Sb_2Te_3 and $Ge_2Sb_2Te_5$-S2 nanosheets exhibit two common features in their phonon spectra: a unique phonon band spreading the whole Brillouin zone at around 2.2 THz and a frequency gap located between 2.2 and 2.3 THz for Sb_2Te_3 and between 2.4 and 2.5 THz for $Ge_2Sb_2Te_5$-S2.

Several studies[56,57] have pointed out that a phonon band gap can lead to high lattice thermal conductivity as certain phonon-phonon scattering processes, specifically two acoustic phonons merging into one optical phonon, become inefficient. In this study, the largest gap value is found in Sb_2Te_3, followed by that of $GeSb_2Te_4$ and that of $Ge_2Sb_2Te_5$-S2. In $Ge_2Sb_2Te_5$-S1, no frequency gap is observed. The gap value

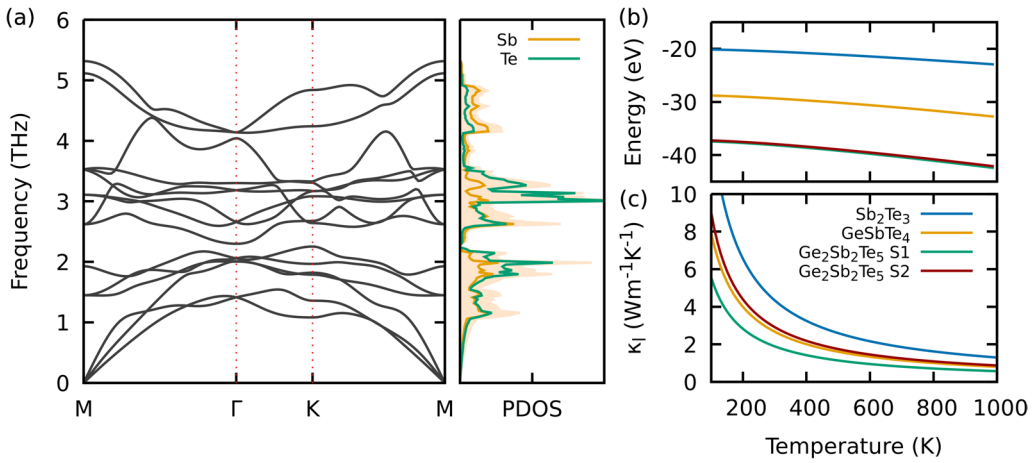

Fig. 2 Calculated dynamic properties: (a) phonon spectrum curves of Sb_2Te_3 and corresponding total DOS (light orange background) and projected DOS (color lines). (b) Calculated Gibbs energy as a function of temperature. (c) Lattice thermal conductivity as a function of temperature obtained from LBTE in the a-axis direction (Color figure online).

aligns with what is described in literature regarding its correlation with the lattice thermal conductivity.

As materials with an energy gap are more amenable to exhibit high lattice thermal conductivity, this type of material is probably not well suited for thermoelectric applications. For the four nanosheets of our study, the band gap is very small. A structural deformation creates differences in rigidity between the modes below and above the band gap, thus modifying the band gap itself.[58] As a consequence, the phonon band gap could be tuned by applying stress. This can indeed be observed in Figs. 3, S9, S10 and S11. When the applied stress is larger than 0.5%, the phonon gap is closed for Sb_2Te_3. In addition, Argaman et al.[58] showed that, in binary chalcogenide compounds, the atomic mass difference increases the band gap by affecting the relative atoms motion. This explains why the frequency gap of Sb_2Te_3 is much smaller than that of Bi_2Te_3.[50] This criterion is however hardly applicable to our nanosheets as we are comparing a binary compound with three ternary compounds and the latter ones contain the same three elements.

Electronic and Transport Properties

From the fully optimized structures, the band structures of Sb_2Te_3, $GeSb_2Te_4$ and $Ge_2Sb_2Te_5$-S1 and -S2 have been calculated with the PBEsol functional[29] and the hybrid HSEsol functional[59] with and without SOC. The band structures are illustrated in Figs. 4 and S12, and the calculated band gaps are gathered in Table III. As can be seen, the effect of SOC is significant for all the compounds. To obtain a more accurate band gap, the hybrid functional incorporating a 25% Hartree-Fock exchange was used to calculate the band structures. This hybrid functional effectively mitigates the issue of band gap underestimation frequently encountered with conventional GGA functionals. Sb_2Te_3, $GeSb_2Te_4$ and $Ge_2Sb_2Te_5$-S1 nanosheets are semiconductors with indirect energy band gap of 0.707 eV, 0.767 eV and 0.739 eV, respectively. Even if gaps are enlarged with HSEsol, the energy gap of $Ge_2Sb_2Te_5$-S2 is nearly zero. Except for the gap energy, the band structures calculated by the PBEsol functional follow a similar trend to those obtained using the HSEsol functional. Consequently, this enables us to calculate the transport properties using the GGA band structure with a dense k-mesh while benefitting from the accurate band gap provided by HSEsol.

In all the three compounds, Sb_2Te_3, $GeSb_2Te_4$, $Ge_2Sb_2Te_5$ (S1 and S2), the conduction band minimum (CBM) is located at the Γ point and the valence band maximum (VBM) is located along the Γ-M direction. Unlike a single conduction band minimum, we observe four, four, six and two valence band maxima located within a narrow energy range of 0.1 eV near the Fermi energy for Sb_2Te_3, $GeSb_2Te_4$, $Ge_2Sb_2Te_5$-S1 and $Ge_2Sb_2Te_5$-S2, respectively. Given the presence of multiple maxima in the valence band, as opposed to the single minimum of the conduction one, the density of states is higher in the valence band. This leads us

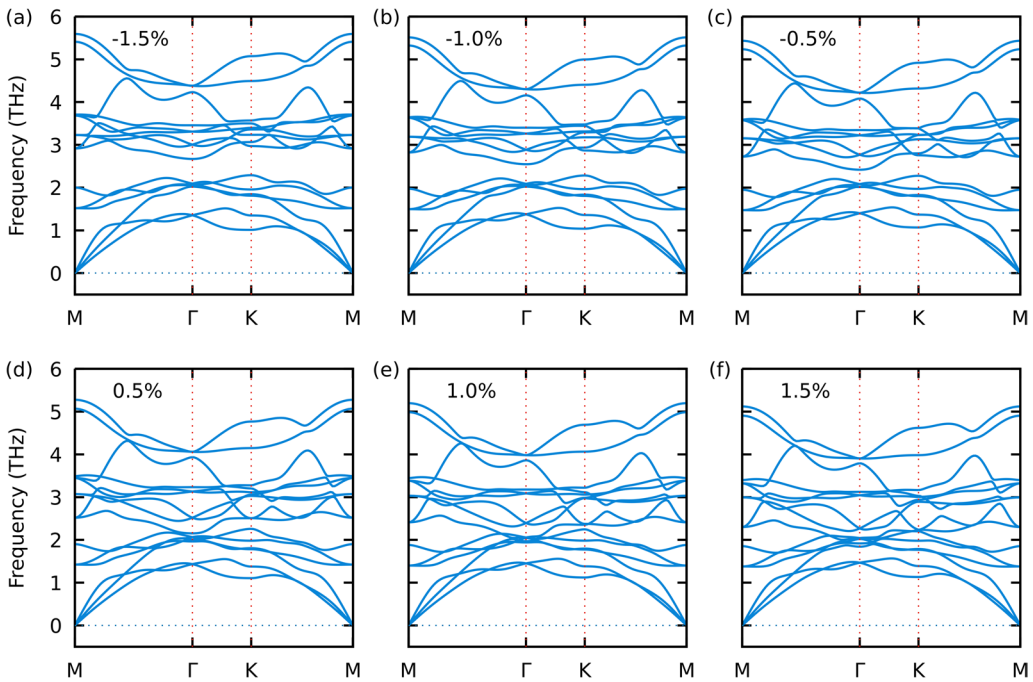

Fig. 3 Phonon spectrum curves of Sb_2Te_3 nanosheets under − 1.5% (a), − 1.0% (b) and − 0.5% (c) compressive strains, and 0.5% (d), 1.0% (e) and 1.5% (f) tensile strains.

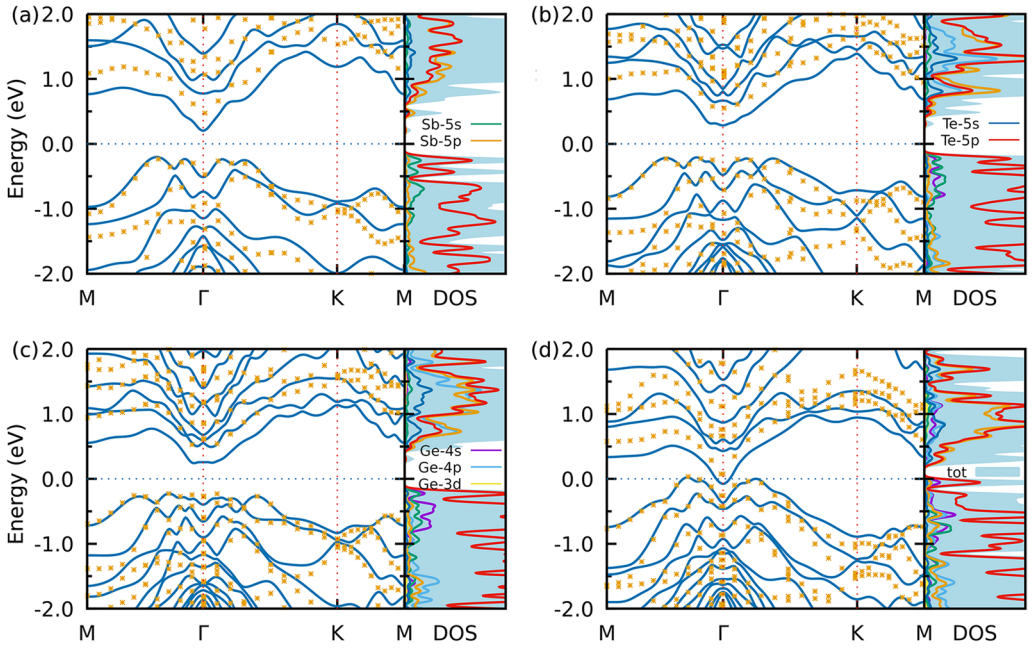

Fig. 4 Electronic band structures of (a) Sb_2Te_3, (b) $GeSb_2Te_4$, (c) $Ge_2Sb_2Te_5$-S1 and (d) $Ge_2Sb_2Te_5$-S2 calculated with PBEsol functional (lines) and HSEsol functional (stars) with spin-orbit coupling.

Table III Electronic parameters of the nanosheets Sb_2Te_3, $GeSb_2Te_4$, and $Ge_2Sb_2Te_5$-S1 and $Ge_2Sb_2Te_5$-S2 calculated with the PBEsol and HSEsol functionals: gap energies (with spin-orbit coupling in parenthesis), deformation potential E_d, elastic constant C_{2D} and carriers effective mass m^* in the a-axis direction.

Compounds	Gap energy (eV)		Carriers	E_d (eV)	C_{2D} (N/m)	m^* (m_e)
	PBEsol	HSEsol				
Sb_2Te_3	0.674 (0.406)	0.997 (0.707)	Holes	6.75	34.02	0.15
			Electrons	8.80		0.11
$GeSb_2Te_4$	0.680 (0.493)	0.984 (0.767)	Holes	8.13	34.24	0.19
			Electrons	8.83		0.21
$Ge_2Sb_2Te_5$-S1	0.654 (0.469)	0.966 (0.739)	Holes	8.21	32.02	0.24
			Electrons	8.81		0.16
$Ge_2Sb_2Te_5$-S2	0.235 (0)	0.495 (0.039)	Holes	8.26	29.63	0.17
			Electrons	10.28		0.12

to expect a higher Seebeck coefficient for p-type materials in accordance with the Mott formula.[60] Achieving a higher value of the thermopower implies the need for higher effective mass at a low carrier concentration range. In general, the presence of highly flat bands and high density of states near the Fermi level contributes to enhancing the thermopower. The analysis of the partial density of states (PDOS) (see Fig. 4) reveals that Te-5p, Sb-5s and Ge-4s orbitals dominate the valence band near the Fermi energy, while the conduction band is dominated by Sb-5p, Ge-4p and Te-5p orbitals.

By solving the Boltzmann transport equation based on the band structures built from a very dense mesh in the full BZ, the Seebeck coefficient S, electrical conductivity σ/τ and electronic part of the thermal conductivity κ_e/τ can be evaluated, the latter two being dependent on the relaxation time due to the use of the RTA approximation. The relaxation time τ depends on the charge carrier concentration, the temperature and the electron energies. To date, due to the lack of experimental values, the determination of relaxation time τ of two-dimensional materials relies on ab initio or empirical methods, which inherently introduce approximations. For simplicity, many studies[45,61] dealing with low-dimensional materials report the use of τ from experimental values of the corresponding bulk structures based on the assumption that similar bonding exists in the slab of thin films and the bulk. Another popular method to evaluate τ is the use of the Takagi formula (Eq. 1), based on the DP theory outcomes and charge carriers effective mass that can be determined from ab initio calculations. The elastic constants, effective mass and deformation potential energy of the compounds of interest have been calculated and the values are reported in Table III. Using this formula, the values of τ/T for holes for

Sb_2Te_3, $GeSb_2Te_4$ and $Ge_2Sb_2Te_5$-S1 and $Ge_2Sb_2Te_5$-S2 are 11.80 ps/K, 6.35 ps/K and 4.68 ps/K and 6.10 ps/K at 300 K, respectively, and those for the electrons are 9.61 ps/K, 5.05 ps/K, 6.31 ps/K and 5.61 ps/K at 300 K, respectively.

From the calculated τ/T, the evolutions of S, σ and κ_e with respect to temperature and doping level for both *p*-type and *n*-type carriers are depicted in Figs. S13 to S18. Concerning Sb_2Te_3, $GeSb_2Te_4$ and $Ge_2Sb_2Te_5$-S1, both the *n*-type and *p*-type nanosheets exhibit relatively high Seebeck coefficient, with an optimum area located at low temperatures (≤ 400 K) and doping levels ($\leq 10^{19}$ cm^{-3}). Despite the lower lattice thermal conductivity of $Ge_2Sb_2Te_5$-S2, its electronic thermal conductivity is much higher than that of the other nanosheets as a result of its metallicity.

The figure of merit (zT) is depicted in Fig. 5 as a function of temperature and hole doping level. For comparison, we have also calculated the temperature-dependent and electron doping level-dependent zT. The results are depicted in Fig. S19. The zT values for *p*-type doped nanosheets are much higher than those for *n*-type nanosheets. The range of temperatures to obtain a high zT value is very wide for Sb_2Te_3, $GeSb_2Te_4$ and $Ge_2Sb_2Te_5$-S1 going from 400 K to 1000 K, whereas the doping level range is relatively narrow spanning from 10^{20} h/cm^3 to 2×10^{21} h/cm^3. Much like the lattice thermal conductivity, the carrier doping level is likewise a bulk characteristic. Therefore, the doping level of the nanosheet is obtained by multiplying the doping level of the bulk by L_z/d (see section on computational details). At last, we have gathered in Table IV the transport properties of the four nanosheets calculated at 300 K, 500 K and 700 K and for a hole doping level at around 3×10^{20} cm^{-3}. The highest values of zT are 2.94, 2.63 and 2.27 for Sb_2Te_3, $GeSb_2Te_4$, and $Ge_2Sb_2Te_5$-S1, respectively, which is obtained at temperatures of 680 K, 790 K and 800 K, and at doping levels of 2.96×10^{20} cm^{-3}, 3.61×10^{20} cm^{-3} and 3.83×10^{20} cm^{-3}, respectively.

The electronic structures of ultra-thin films are highly responsive to external stimuli, chemical modification, and mechanical deformations.[62] To evidence the strain effect on the electronic structure, the band structures and DOS of the strained and unstrained nanosheets are shown in Fig. 6a. The energy gap decreases slightly as the applied strain increases although not leading to a semiconductor–metal transition. The energy difference between the VBM and the second to fourth highest VB of Sb_2Te_3 is 30 meV, 31 meV and 46 meV for unstrained Sb_2Te_3. By

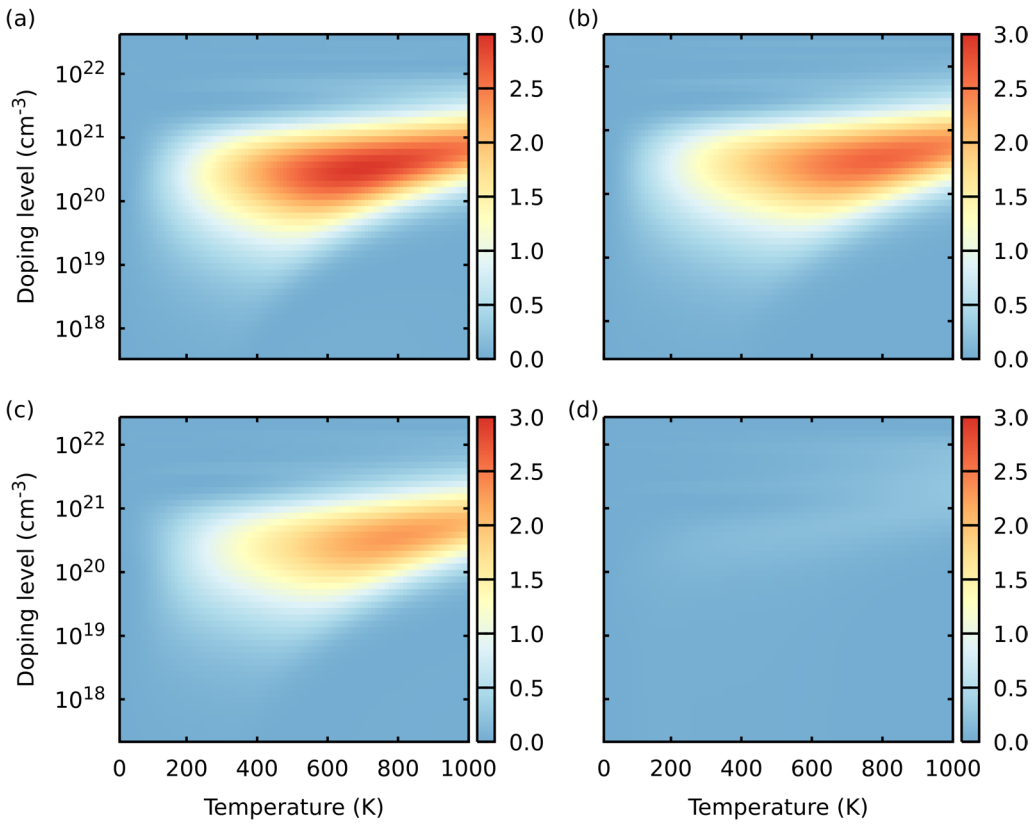

Fig. 5 Figure of merit (zT) of (a) Sb_2Te_3, (b) $GeSb_2Te_4$, (c) $Ge_2Sb_2Te_5$-S1 and (d) $Ge_2Sb_2Te_5$-S2 in the *a*-axis direction as a function of temperature and *p*-type carriers doping level.

Table IV Transport properties of the Sb_2Te_3, $GeSb_2Te_4$, and $Ge_2Sb_2Te_5$-S1 and $Ge_2Sb_2Te_5$ -S2 nanosheets at 300K, 500K and 700K and at a hole doping level of 3×10^{20} cm^{-3}.

	τ			σ			S			κ			zT		
	300	500	700	300	500	700	300	500	700	300	500	700	300	500	700
Sb_2Te_3	39.3	23.6	16.9	6.92	3.62	2.33	221.7	249.4	270.5	6.74	4.54	4.07	1.51	2.48	2.93
$GeSb_2Te_4$	21.2	12.7	9.1	2.72	1.39	0.88	240.0	262.4	282.4	3.46	2.28	1.92	1.36	2.10	2.57
S1	15.6	9.4	6.7	1.73	0.81	0.50	223.9	259.2	283.6	2.46	1.57	1.29	1.06	1.74	2.18
S2	20.3	12.2	8.7	3.56	2.13	1.58	79.9	79.0	70.8	5.56	4.90	5.47	0.12	0.14	0.10

τ is the relaxation time in fs, σ is electrical conductivity in units of 10^5 $\Omega^{-1}m^{-1}$, S is the Seebeck coefficient in μV/K and κ is the total (electronic + lattice) thermal conductivity in W $m^{-1}K^{-1}$

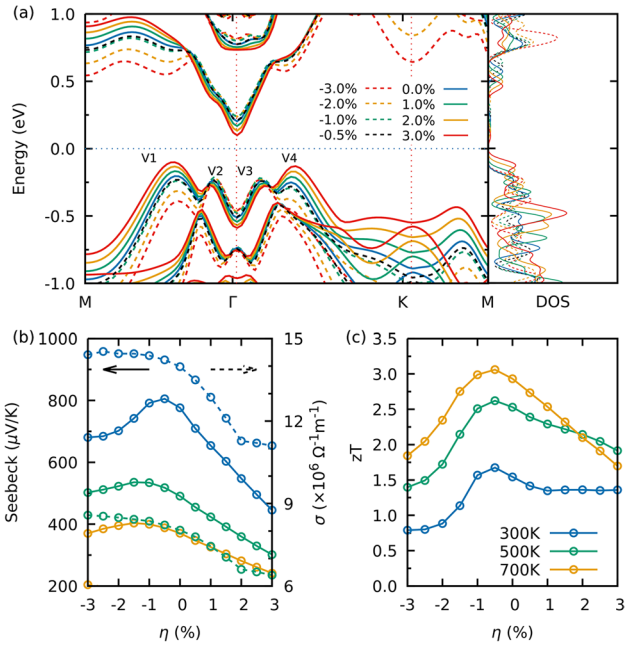

Fig. 6 Evolution of the electronic and thermoelectric properties of Sb_2Te_3 under strains: (a) band structure; (b) Seebeck coefficient and electrical conductivity; (c) figure of merit (zT).

applying biaxial strain, the valence bands become tunable. The degeneracy of VBM N_v at the Fermi level is 6, since there are four maxima in the valence band, the highest degeneracy could be 24. However, this value cannot be reached, as V1 and V4 increase, while V2 and V3 increase at first and then decrease with the increase of applied strain. Under − 0.5% stress in the *a*-axis direction, the degeneracy N_v reaches 18, and as expected, the value of the Seebeck coefficient is maximum for this strain at low temperature (300 K, see Fig. 6b). One can also note that zT reaches a maximum value at this strain for all the temperatures (Fig. 6c). As to the $GeSb_2Te_4$ and $Ge_2Sb_2Te_5$ -S1 nanosheets, the evolution of the band structures under strains is more complex (Fig. S20). The largest degeneracy is obtained for a tensile strain of around 0.5% to 1.0%, which coincide with the region where both the Seebeck coefficient and zT are maximum (Fig. S21a, b, c, d).

The TE performances of Sb_2Te_3, $GeSb_2Te_4$, $Ge_2Sb_2Te_5$ -S1 and $Ge_2Sb_2Te_5$-S2 under strain is shown in Figs. 6b, c, S21 and S22. Due to the change of CBM energy at the Γ point, the effective carrier mass, derived from single-band approximation, varies under applied strains. However, calculating the scattering time for each individual case would be computationally challenging, so we have kept the relaxation time τ from the fully relaxed structures.

The Seebeck coefficient decreases when either compressive or tensile strains are applied to the nanosheets. The degradation is much more stringent under tensile strains. The Seebeck coefficient and electrical conductivity are known to evolve oppositely according to the Mott formula.[60] This behavior is well followed under compressive strains where the electrical conductivity is improved while the Seebeck coefficient degrades, but not under tensile strains where both the electrical conductivity and the Seebeck coefficient decrease. Hence, this result suggests that applying strains to materials could be a route to decorrelate the electrical conductivity and the Seebeck coefficient, potentially improving both.

Whereas both the Seebeck coefficient and electrical conductivity are mostly degraded under tensile strain, the figure of merit is strongly decreased under compressive strains and less under tensile strains. This behavior can be explained by observing the evolution of the electronic thermal conductivity (Fig. S21) under strains. Indeed, for all the nanosheets except $Ge_2Sb_2Te_5$-S2, which is metallic, the electronic thermal conductivity monotonically decreases from -3% compressive strain to +3% tensile strain. This trend is the same as that of the electrical conductivity, as expected from the Wiedemann-Franz law, but seems much more stringent that in the case of the electrical conductivity. Consequently, the high electronic thermal conductivity under compressive strains is deleterious to zT, but much less so under tensile strains. The lattice thermal conductivity is also expected to play a role in the evolution of zT but due to the very significant computing overload of calculating the lattice thermal conductivity under all the strains using the linearized Boltzmann transport equation, we did not perform these calculations. The zT values are hence calculated with the lattice thermal conductivity of the unstrained structures. However,

one can observe that, according to Zhang et al.[63], strains applied to nanoribbons of graphene decrease the lattice thermal conductivity, which is beneficial to the thermoelectric figure of merit, although graphene nanoribbons are very different materials from ours. Nonetheless, other investigations undertaken on, e.g., KAgSe[64] and InSe[65] have shown similar results. Consequently, it seems to be a very general trend, and if one admits the same behavior for our compounds, the lattice thermal conductivity without strains (that we have used to calculate the zT of the strained compounds) is an upper limit to the values under strains, and the zT presented in Figs. 6 and S22 could be considered as lower bounds.

The TE performances of the nanosheets of Sb_2Te_3, $GeSb_2Te_4$ and $Ge_2Sb_2Te_5$-S1 are seemingly excellent, ranging between 1.5 and 2.5 at 500 K under slight compressive strain (for the former nanosheet) or tensile one (for the latter two). However, the strain effects are not as significant as that in Pb–Bi–Te nanosheets,[45] which could be explained by the fact that the band alignment in the Ge–Sb–Te nanosheets is almost reached for the unstrained structures.

Conclusions

In this work, we have investigated the electronic structure, the TE properties and the stability of some Ge–Sb–Te nanosheets. Four structures, Sb_2Te_3, $GeSb_2Te_4$, $Ge_2Sb_2Te_5$ -S1 and $Ge_2Sb_2Te_5$-S2 have been considered. Sb_2Te_3, $GeSb_2Te_4$ and $Ge_2Sb_2Te_5$-S1 are narrow-gap semiconductors with indirect band gap and are energetically and dynamically stable without strain. $Ge_2Sb_2Te_5$-S2 shows clearly metallic properties. To go beyond the relaxation time approximation, τ has been evaluated using the effective mass approximation and the DP theory. The highest zT values of Sb_2Te_3, $GeSb_2Te_4$ and $Ge_2Sb_2Te_5$-S1 at 700 K with *p*-type doping in *a*-axis direction are 2.94, 2.63 and 2.27, respectively. The strain induced effects on transport properties for the Ge–Sb–Te nanosheets are less pronounced compared to those of Pb–Bi–Te, as the alignment of the valence bands maxima for the four nanosheets is almost reached in the unstrained structures. Under small compressive strains, the phonon frequency gap disappears which would decrease the lattice thermal conductivity. In addition, the Seebeck coefficients of all the semi-conducting nanosheets are enhanced under slight compressive or tensile strains of no more than ±1.0%. Consequently, the nanosheets exhibit excellent TE properties, making them potentially promising candidates for TE applications.

Supplementary Information The online version contains supplementary material available at https://doi.org/10.1007/s11664-024-11134-5.

Acknowledgments This work was granted access to the HPC resources of TGCC under the allocation A0130806881 made by GENCI. It was also granted access to the HPC resources of the Aix-Marseille University.

Funding This work received no funding.

Conflict of interest The authors declare that they have no conflict of interest.

References

1. B. Orr, A. Akbarzadeh, M. Mochizuki, and R. Singh, A review of car waste heat recovery systems utilising thermoelectric generators and heat pipes, Appl. Therm. Eng. **101**, 490–495 (2016)
2. M. Papapetrou, G. Kosmadakis, A. Cipollina, U. La Commare, and G. Micale, Industrial waste heat: Estimation of the technically available resource in the EU per industrial sector, temperature level and country, Appl. Therm. Eng. **138**, 207–216 (2018)
3. G. Fan, K. Liu, H. Su, Y. Luo, Y. Geng, L. Chen, B. Wang, Z. Mao, X. Sui, and X. Feng, Mesoscopic confined ionic thermoelectric materials with excellent ionic conductivity for waste heat harvesting, Chem. Eng. J. **434**, 134702 (2022)
4. R. Aridi, J. Faraj, S. Ali, T. Lemenand, and M. Khaled, Thermoelectric power generators: state-of-the-art, heat recovery method, and challenges, Electricity **2**, 359–386 (2021)
5. I. Petsagkourakis, K. Tybrandt, X. Crispin, I. Ohkubo, N. Satoh, and T. Mori, Thermoelectric materials and applications for energy harvesting power generation, Sci. Technol. Adv. Mater. **19**, 836–862 (2018)
6. M. Sajid, I. Hassan, and A. Rahman, An overview of cooling of thermoelectric devices, Renew. Sustain. Energy Rev. **78**, 15–22 (2017)
7. C.B. Vining, An inconvenient truth about thermoelectrics, Nat. Mater. **8**, 83–85 (2009)
8. C. Tan, X. Cao, X.-J. Wu, Q. He, J. Yang, X. Zhang, J. Chen, W. Zhao, S. Han, G.-H. Nam, M. Sindoro, and H. Zhang, Recent advances in ultrathin two-dimensional nanomaterials, Chem. Rev. **117**, 6225–6331 (2017)
9. D.D. Fan, H.J. Liu, L. Cheng, P.H. Jiang, J. Shi, and X.F. Tang, MoS_2 nanoribbons as promising thermoelectric materials, Appl. Phys. Lett. **105**, 133113 (2014)
10. J. Wu, H. Schmidt, K.K. Amara, X. Xu, G. Eda, and B. Özyilmaz, Large thermoelectricity via variable range hopping in chemical vapor deposition grown single-layer MoS_2, Nano Lett. **14**, 2730–2734 (2014)
11. Y. Hu, T. Yang, D. Li, G. Ding, C. Dun, D. Wu, and X. Wang, Origins of minimized lattice thermal conductivity and enhanced thermoelectric performance in WS_2/WSe_2 lateral superlattice, ACS Omega **6**, 7879–7886 (2021)
12. J. Wang, X.-H. Cao, Y.-J. Zeng, N.-N. Luo, L.-M. Tang, and K.-Q. Chen, Excellent thermoelectric properties of monolayer MoS_2-$MoSe_2$ aperiodic superlattices, Appl. Surf. Sci. **612**, 155914 (2023)
13. S. Kumar and U. Schwingenschlögl, Thermoelectric response of bulk and monolayer $MoSe_2$ and WSe_2, Chem. Mater. **27**, 1278–1284 (2015)
14. R. Venkatasubramanian, E. Siivola, T. Colpitts, and B. O'Quinn, Thin-film thermoelectric devices with high room-temperature figures of merit, Nature **413**, 597–602 (2001)
15. L.M. Gonçalves, C. Couto, P. Alpuim, D.M. Rowe, and J.H. Correia, Thermoelectric properties of Bi_2Te_3/Sb_2Te_3 thin films, Mater. Sci. Forum **514–516**, 156–160 (2006)
16. Y. Pei, X. Shi, A. LaLonde, H. Wang, L. Chen, and G.J. Snyder, Convergence of electronic bands for high performance bulk thermoelectrics, Nature **473**, 66–69 (2011)

17. F. Hao, P. Qiu, Y. Tang, S. Bai, T. Xing, H.-S. Chu, Q. Zhang, P. Lu, T. Zhang, D. Ren, J. Chen, X. Shi, and L. Chen, High efficiency Bi_2Te_3-based materials and devices for thermoelectric power generation between 100 and 300°C, Energy Environ. Sci. **9**, 3120–3127 (2016)
18. L.-D. Zhao, G. Tan, S. Hao, J. He, Y. Pei, H. Chi, H. Wang, S. Gong, H. Xu, V.P. Dravid, C. Uher, G.J. Snyder, C. Wolverton, and M.G. Kanatzidis, Ultrahigh power factor and thermoelectric performance in hole-doped single-crystal SnSe, Science **351**, 141–144 (2015)
19. J. Li, X. Zhang, Z. Chen, S. Lin, W. Li, J. Shen, I.T. Witting, A. Faghaninia, Y. Chen, A. Jain, L. Chen, G.J. Snyder, and Y. Pei, Low-symmetry rhombohedral GeTe thermoelectrics, Joule **2**, 976–987 (2018)
20. J. Lee, S. Kim, R. Jeyasingh, M. Asheghi, H.S.P. Wong, and K.E. Goodson, Microthermal stage for electrothermal characterization of phase-change memory, IEEE Electron. Device Lett. **32**, 952–954 (2011)
21. T.-R. Wei, P. Hu, H. Chen, K. Zhao, P. Qiu, X. Shi, and L. Chen, Quasi-two-dimensional GeSbTe compounds as promising thermoelectric materials with anisotropic transport properties, Appl. Phys. Lett. **114**, 053903 (2019)
22. P. Chen, H. Wu, B. Zhang, Z. Zhou, S. Zheng, L. Dai, Y. Huo, D. Zhang, Y. Yan, K. Peng, G. Han, X. Lu, X. Zhou, and G. Wang, Intrinsically low lattice thermal conductivity and anisotropic thermoelectric performance in in-doped $GeSb_2Te_4$ single crystals, Adv. Funct. Mater. **33**, 2211281 (2023)
23. J. Jiang, L. Chen, S. Bai, Q. Yao, and Q. Wang, Thermoelectric properties of p-type $(Bi_2Te_3)_x(Sb_2Te_3)_{1-x}$ crystals prepared via zone melting, J. Crys. Growth **277**, 258–263 (2005)
24. B. Xu, J. Zhang, G. Yu, S. Ma, Y. Wang, and Y. Wang, Thermoelectric properties of monolayer Sb_2Te_3, J. Appl. Phys. **124**, 165104 (2018)
25. W.-Y. Fang, X.-X. Rao, J. Cheng, P. Xue, X.-F. Sheng, C.-J. Liu, and P.-C. Zhang, Theoretical investigation of the electronic structure and thermoelectric performance of 2D $GeSb_2Te_4$ and $GeBi_2Te_4$, Vacuum **216**, 112490 (2023)
26. P.E. Blöchl, Projector augmented-wave method, Phys. Rev. B **50**, 17953 (1994)
27. G. Kresse and J. Furthmüller, Efficient iterative schemes for ab initio total-energy calculations using a plane-wave basis set, Phys. Rev. B **54**, 11169–11186 (1996)
28. G. Kresse and J. Hafner, Norm-conserving and ultrasoft pseudopotentials for first-row and transition elements, J. Phys. Cond. Matter. **6**, 8245–8257 (1994)
29. J.P. Perdew, A. Ruzsinszky, G.I. Csonka, O.A. Vydrov, G.E. Scuseria, L.A. Constantin, X. Zhou, and K. Burke, Restoring the density-gradient expansion for exchange in solids and surfaces, Phys. Rev. Lett. **100**, 136406 (2008)
30. S. Baroni, S. de Gironcoli, A. Dal Corso, and P. Giannozzi, Phonons and related properties of extended systems from density-functional perturbation theory, Rev. Mod. Phys. **73**, 515–562 (2001)
31. A. Togo, First-principles phonon calculations with phonopy and phono3py, J. Phys. Soc. Jpn. **92**, 012001 (2023)
32. A. Togo, L. Chaput, T. Tadano, and I. Tanaka, Implementation strategies in phonopy and phono3py, J. Phys. Condens. Matter **35**, 353001 (2023)
33. L. Chaput, Direct solution to the linearized phonon Boltzmann equation, Phys. Rev. Lett. **110**, 265506 (2013)
34. S.-D. Guo, Phonon transport of Janus monolayer MoSSe: a first-principles study, Phys. Chem. Chem. Phys. **20**, 7236–7242 (2018)
35. G.K.H. Madsen, J. Carrete, and M.J. Verstraete, BoltzTraP2, a program for interpolating band structures and calculating semi-classical transport coefficientsk, Comput. Phys. Commun. **231**, 140–145 (2018)
36. J. Bardeen and W. Shockley, Deformation potentials and mobilities in non-polar crystals, Phys. Rev. **80**, 72–80 (1950)
37. R. Xu, X. Zou, B. Liu, and H.-M. Cheng, Computational design and property predictions for two-dimensional nanostructures, Mater. Today **21**, 391–418 (2018)
38. A.D. Becke and K.E. Edgecombe, A simple measure of electron localization in atomic and molecular systems, J. Chem. Phys. **92**, 5397–5403 (1990)
39. R.F.W. Bader, *Atoms in Molecules: A Quantum Theory. International Series of Monographs on Chemistry* (Clarendon Press, Oxford,1990)
40. R. Dronskowski and P.E. Blöchl, Crystal orbital Hamilton populations (COHP): energy-resolved visualization of chemical bonding in solids based on density-functional calculations, J. Phys. Chem. **97**, 8617–8624 (1993)
41. A. Otero-de-la Roza, E.R. Johnson, and V. Luaña, Critic2: a program for real-space analysis of quantum chemical interactions in solids, Comput. Phys. Commun. **185**, 1007–1018 (2014)
42. R. Nelson, C. Ertural, J. George, V.L. Deringer, G. Hautier, and R. Dronskowski, LOBSTER: local orbital projections, atomic charges, and chemical-bonding analysis from projector-augmented-wave-based density-functional theory, J. Comput. Chem. **41**, 1931–1940 (2020)
43. K. Momma and F. Izumi, VESTA3 for three-dimensional visualization of crystal, volumetric and morphology data, J. Appl. cryst. **44**, 1272–1276 (2011)
44. N. Mounet, M. Gibertini, P. Schwaller, D. Campi, A. Merkys, A. Marrazzo, T. Sohier, I.E. Castelli, A. Cepellotti, G. Pizzi, and N. Marzari, Two-dimensional materials from high-throughput computational exfoliation of experimentally known compounds, Nat. Nanotechnol. **13**, 246–252 (2018)
45. W. Ma, J. Tian, P. Boulet, and M.-C. Record, First-principle investigations on the electronic and transport properties of $PbBi_2Te_2X_2$ (X = S/Se/Te) monolayers, Nanomaterials **11**, 2979 (2021)
46. X. Chen, H.D. Zhou, A. Kiswandhi, I. Miotkowski, Y.P. Chen, P.A. Sharma, A.L. Lima Sharma, M.A. Hekmaty, D. Smirnov, and Z. Jiang, Thermal expansion coefficients of Bi_2Se_3 and Sb_2Te_3 crystals from 10 K to 270 K, Appl. Phys. Lett. **99**, 261912 (2011)
47. J. Feng, A. Lotnyk, H. Bryja, X. Wang, M. Xu, Q. Lin, X. Cheng, M. Xu, H. Tong, and X. Miao, "Stickier''-surface Sb_2Te_3 templates enable fast memory switching of phase change material $GeSb_2Te_4$ with growth-dominated crystallization, ACS Appl. Mater. Interf. **12**, 33397–33407 (2020)
48. C.F. Matta and R.J. Boyd, "Stickier''-surface Sb_2Te_3 templates enable fast memory switching of phase change material $GeSb_2Te_4$ with growth-dominated crystallization. In *The Quantum Theory of Atoms in Molecules*, vol.1–34, ed. by C.F. Matta and R.J. Boyd (Wiley-VCH Verlag GmbH & Co. KGaA, Weinheim, 2007)
49. C. Gatti and Z. Kristallog, Chemical bonding in crystals: new directions, Crystal. Mater. **220**, 399–457 (2005)
50. W. Ma, M.-C. Record, J. Tian, and P. Boulet, Influence of the stacking sequence on layered-chalcogenide properties: first principles investigation of $Pb_2Bi_2Te_5$, Phys. Chem. Chem. Phys. **23**, 11300–11313 (2021)
51. J. Zhang, L. Song, M. Sist, K. Tolborg, and B.B. Iversen, Chemical bonding origin of the unexpected isotropic physical properties in thermoelectric Mg_3Sb_2 and related materials, Nat. Commun. **9**, 4716 (2018)
52. G.A. Slack, Nonmetallic crystals with high thermal conductivity, J. Phys. Chem. Solids **34**, 321–335 (1973)
53. M.T. Dove (ed.), *Introduction to Lattice Dynamics* (Cambridge University Press, Cambridge, 1993)
54. J. Tian, W. Ma, P. Boulet, and M.-C. Record, Electronic and transport properties of strained and unstrained $Ge_2Sb_2Te_5$: a DFT investigation, Materials **16**, 5015 (2023)

55. G. Ding, Y. Hu, D. Li, and X. Wang, A comparative study of thermoelectric properties between bulk and monolayer SnSe, Res. Phys. **15**, 102631 (2019)
56. L. Lindsay, D.A. Broido, and T.L. Reinecke, First-principles determination of ultrahigh thermal conductivity of boron arsenide: a competitor for diamond? Phys. Rev. Lett. **111**, 025901 (2013)
57. J. Sang Kang, M. Li, H. Wu, H. Nguyen, and Y. Hu, Experimental observation of high thermal conductivity in boron arsenide, Science **361**, 575–578 (2018)
58. U. Argaman, R.E. Abutbul, Y. Golan, and G. Makov, Phonon band gaps in the IV–VI monochalcogenides, Phys. Rev. B **100**, 054104 (2019)
59. L. Schimka, J. Harl, and G. Kresse, Improved hybrid functional for solids: the HSEsol functional, J. Chem. Phys. **134**, 024116 (2011)
60. M. Jonson and G.D. Mahan, Mott's formula for the thermopower and the Wiedemann–Franz law, Phys. Rev. B **21**, 4223–4229 (1980)
61. M.R. Diznab, I. Maleki, S.M. Vaez Allaei, Y. Xia, and S.S. Naghavi, Achieving an ultrahigh power factor in Sb_2Te_2Se monolayers via valence band convergence, ACS Appl. Mater. Interfaces **11**, 46688–46695 (2019)
62. J. Liu, D.D. Cannon, K. Wada, Y. Ishikawa, D.T. Danielson, S. Jongthammanurak, J. Michel, and L.C. Kimerling, Deformation potential constants of biaxially tensile stressed Ge epitaxial films on Si(100), Phys. Rev. B **70**, 155309 (2004)
63. G. Zhang and Y.-W. Zhang, Strain effects on thermoelectric properties of two-dimensional materials. Mech. Mater. **91**, 382–398 (2015)
64. Z. Xu, Q. Xia, and G. Gao, A strain-induced considerable decrease of lattice thermal conductivity in 2D KAgSe with Coulomb interaction, Phys. Chem. Chem. Phys. **24**, 24917 (2022)
65. Q. Wang, L. Han, L. Wu, T. Zhang, S. Li, and P. Lu, Strain effect on thermoelectric performance of InSe monolayer, Nano Res. Lett. **14**, 287 (2019)